2018 IEEE 15th International Symposium on Biomedical Imaging (ISBI 2018)
April 4-7, 2018, Washington, D.C., USA

PHASELESS DIFFRACTION TOMOGRAPHY WITH REGULARIZED BEAM PROPAGATION

Thanh-an Pham⋆*, Emmanuel Soubies*⋆*, Joowon Lim*†*,*
Alexandre Goy†*, Ferréol Soulez*‡*, Demetri Psaltis*†*, and Michael Unser*⋆

⋆ *Biomedical Imaging Group, Ecole polytechnique fédérale de Lausanne (EPFL), 1015 Lausanne, Switzerland*
† *Optics Laboratory, Ecole polytechnique fédérale de Lausanne (EPFL), 1015 Lausanne, Switzerland*
‡ *Univ Lyon, Univ Lyon1, Ens de Lyon, CNRS, Centre de Recherche Astrophysique de Lyon UMR5574, F-69230, Saint-Genis-Laval, France.*

ABSTRACT

In recent years, researchers have obtained impressive reconstructions of the refractive index (RI) of biological objects through the combined use of advanced physics (nonlinear forward model) and regularization. Here, we propose an adaptation of these techniques for the more challenging problem of intensity-only measurements. It involves a difficult nonconvex optimization problem where phase and distribution of the RI must be jointly estimated. Using an adequate splitting, we leverage recent achievements in phase retrieval and RI reconstruction to perform this task. This yields an efficient reconstruction method with sparsity constraints.

***Index Terms*—** Beam propagation, intensity measurement, coherence tomography, image reconstruction.

1. INTRODUCTION

Having access to the map of the refractive index (RI) of biological samples has a broad range of applications [1]. It can be obtained through optical diffraction tomography (ODT). There, the sample is illuminated by a set of tilted incident waves and holographic measurements of the resulting scattered fields are recorded (see Figure 1). The RI distribution is then recovered by solving an inverse scattering problem.

Pioneering works to solve the recovery problem were relying on direct linear inversion algorithms such as back-propagation [2, 3]. Reconstructions were then dramatically improved using regularization-based methods [4, 5]. However, the validity of linear models is restricted to weakly scattering samples. To overcome this limitation, the most recent reconstruction algorithms combine advanced physical models with modern regularization [6, 7]. These methods account for multiple scattering, which opens the door to the imaging of strongly scattering objects.

As a CCD camera can measure intensity only, holographic measurements must be acquired using an elaborate interferometric setup that needs a reference beam or multiple measurements per angle. Phaseless diffraction tomography allows one to simplify this setup by recording a single intensity measurement per angle. However, this comes at the price of a more challenging inverse problem. Existing methods tackle this difficulty by alternating between phase retrieval and RI estimation. The phase estimation step is generally performed using the popular Gerchberg-Saxton projection [8]. The RI reconstruction step has known the same progression as for classical ODT, going from linear models [9, 10] to nonlinear ones with ad hoc regularization [11, 12, 13].

This research was supported by the European Research Council (ERC) under the European Union's Horizon 2020 research and innovation programme, Grant Agreement no. 692726 "GlobalBioIm: Global integrative framework for computational bio-imaging." Funding: European Research Council (ERC) (692726).

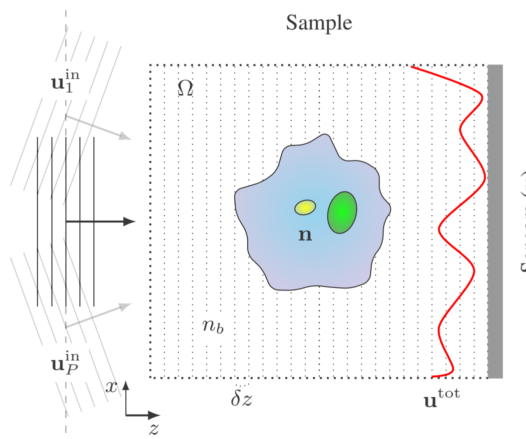

Fig. 1. Diffraction-tomography setup. A sample of RI $\mathbf{n} = n_b\mathbf{1} + \delta\mathbf{n}$ is immersed in a background medium of index n_b and impinged by a set of incident waves $(\mathbf{u}_p^{\text{in}})_{p\in[1\ldots P]}$. The interaction of the wave with the object produces a total field $\mathbf{u}^{\text{tot}}$. Its squared magnitude is recorded by the detector.

Contributions In this paper, we propose phaseless diffraction tomography as an adaptation of the efficient regularized method [6] that solves inverse scattering. We thereby leverage the benefit of an advanced nonlinear physical model and sparse regularization. We first express the inverse problem within a variational framework that includes the total variation (TV) penalty together with a nonnegativity constraint. Then, using an adequate splitting strategy, we carry out the optimization by alternating between simpler steps. For each subproblem, we deploy an efficient numerical solution. Finally, we validate the proposed method on simulated and experimental data.

2. BEAM-PROPAGATION METHOD

We consider the 2D area Ω discretized in $(N_{\text{x}} \times N_{\text{z}})$ points with steps δx and δz. We denote the RI distribution of the sample by $\mathbf{n} \in \mathbb{R}^{N_{\text{x}}\times N_{\text{z}}}$ and the RI of the surrounding medium by $n_b \in \mathbb{R}$. Also, we introduce the RI variation $\delta\mathbf{n} = (\mathbf{n} - n_b\mathbf{1})$ with $\mathbf{1} = \sum_{k=1}^{N_{\text{x}}N_{\text{z}}} \mathbf{e}_k$. The incident plane wave of wavelength λ is referred to as $\mathbf{u}^{\text{in}} \in \mathbb{C}^{N_{\text{x}}\times N_{\text{z}}}$. We represent the total field $\mathbf{u}^{\text{tot}}(\delta\mathbf{n}) \in \mathbb{C}^{N_{\text{x}}\times N_{\text{z}}}$ (incident + scattered) as

$$\mathbf{u}_q^{\text{tot}}(\delta\mathbf{n}) = \mathbf{a}_q(\delta\mathbf{n})\,\mathrm{e}^{\mathrm{j}k_b q}, \tag{1}$$

where $\mathbf{a}(\delta\mathbf{n}) \in \mathbb{C}^{N_x \times N_z}$ is the complex envelope of the wave, $k_b = \frac{2\pi n_b}{\lambda}$ is the background wavenumber, and the index q denotes the z slice of the corresponding matrix. The beam-propagation method (BPM) computes $\mathbf{a}(\delta\mathbf{n})$ slice-by-slice along the optical axis z using the recursive relation

$$\mathbf{a}_q(\delta\mathbf{n}) = (\mathbf{a}_{q-1}(\delta\mathbf{n}) * \mathbf{h}_{\text{prop}}) \odot \mathbf{p}_q(\delta\mathbf{n}), \quad (2)$$

$$\mathbf{a}_0(\delta\mathbf{n}) = \mathbf{u}_0^{\text{in}}, \quad (3)$$

where $\odot$ denotes the Hadamard product and $*$ the convolution operation. In (2), $\mathbf{a}_{q-1}(\delta\mathbf{n})$ is first propagated to the next slice by convolution with the propagation kernel $\mathbf{h}_{\text{prop}} \in \mathbb{C}^{N_x}$ given by

$$\mathbf{h}_{\text{prop}} = \mathcal{F}^{-1}\left\{\exp\left(\frac{-\mathrm{j}\boldsymbol{\omega}^2\delta z}{k_b + \sqrt{{k_b}^2 - \boldsymbol{\omega}^2}}\right)\right\} \text{ (diffraction step)}, \quad (4)$$

where $\mathcal{F}$ is the 1D discrete Fourier transform, $\boldsymbol{\omega} \in \mathbb{R}^{N_x}$ is the frequency variable for the x direction, and all operations are component-wise. This convolution is followed by a point-wise multiplication with the qth slice of the phase mask $\mathbf{p}(\delta\mathbf{n}) \in \mathbb{C}^{Nx \times Nz}$ defined as

$$\mathbf{p}_q(\delta\mathbf{n}) = \exp\left(\mathrm{j}k_0\delta z(\delta\mathbf{n})_q\right) \quad \text{(refraction step)}, \quad (5)$$

where $k_0 = k_b/n_b$ is the wavenumber in free space. Finally, the BPM forward model is defined by the operator

$$\begin{aligned} \mathrm{B}: \quad \mathbb{R}^{N_x \times N_z} &\to \mathbb{C}^{N_x} \\ \delta\mathbf{n} &\mapsto \mathbf{a}_{N_z}(\delta\mathbf{n})\, \mathrm{e}^{\mathrm{j}k_b N_z}, \end{aligned} \quad (6)$$

where $\mathbf{a}_{N_z}(\delta\mathbf{n}) \in \mathbb{C}^{N_x}$ is computed using (2)-(3).

3. ADMM-BASED RECONSTRUCTION

We denote by P the number of the incident planes waves $\mathbf{u}_p^{\text{in}}\ \forall\, p \in [1 \ldots P]$. The forward model that links $\delta\mathbf{n}$ to the intensity measurements $\mathbf{y}_p \in \mathbb{R}^{N_x}$ is

$$\mathbf{y}_p = |\mathrm{B}_p(\delta\mathbf{n})|^2 + \mathbf{s}_p\ \forall\, p \in [1 \ldots P], \quad (7)$$

where $\mathbf{s}_p \in \mathbb{R}^{N_x}$ is a vector of noise components, $|\cdot|$ denotes the component-wise magnitude, $(\cdot)^2$ denotes the component-wise square operation, and B_p is the BPM model in (6) associated to $\mathbf{u}_p^{\text{in}}$. To recover the RI variation $\delta\mathbf{n}$, we minimize the TV-regularized negative log-likelihood of the noise distribution

$$\widehat{\delta\mathbf{n}} \in \left\{\arg\min_{\delta\mathbf{n}\in\chi}\left(\frac{1}{2}\sum_{p=1}^{P}\||\mathrm{B}_p(\delta\mathbf{n})|^2 - \mathbf{y}_p\|_{\mathbf{W}_p}^2 + \tau\|\delta\mathbf{n}\|_{\text{TV}}\right)\right\}, \quad (8)$$

with τ a regularization parameter, $\chi \subseteq \mathbb{R}_{\geq\mathbf{0}}^{N_x \times N_z}$ a set that enforces the nonnegativity constraint, $\mathbf{W}_p = \mathbf{diag}((w_1^p, \ldots, w_{N_x}^p)) \in \mathbb{R}^{N_x \times N_x}$ a diagonal matrix, and $\|\cdot\|_{\mathbf{W}}$ a weighted ℓ_2-norm such that $\|\mathbf{v}\|_{\mathbf{W}}^2 = \sum_{m=1}^{N_x} w_m^p(\mathbf{v}_m)^2$. To account for shot noise (Poisson), we set these weights to the inverse of the intensity of each measurement.

We then apply the popular alternating direction method of multipliers (ADMM) [14] strategy to solve our inverse problem. The leading idea is to split the initial problem in a series of simpler subproblems for which we can deploy efficient algorithms. Starting from (8), we introduce the auxiliary variables $\mathbf{v}_p \in \mathbb{C}^{N_x} \forall\, p \in [1 \ldots P]$ to obtain the equivalent constrained problem

$$\widehat{\delta\mathbf{n}} \in \arg\min_{\delta\mathbf{n}\in\chi}\left(\frac{1}{2}\sum_{p=1}^{P}\||\mathbf{v}_p|^2 - \mathbf{y}_p\|_{\mathbf{W}_p}^2 + \tau\|\delta\mathbf{n}\|_{\text{TV}}\right),$$
$$\text{s.t. } \mathbf{v}_p = \mathrm{B}_p(\delta\mathbf{n}) \quad \forall p \in [1 \ldots P]. \quad (9)$$

This problem admits the augmented-Lagrangian form

$$\mathcal{L}(\delta\mathbf{n}, \mathbf{v}_1, \ldots, \mathbf{v}_P, \mathbf{w}_1, \ldots, \mathbf{w}_P) = \frac{1}{2}\sum_{p=1}^{P}\||\mathbf{v}_p|^2 - \mathbf{y}_p\|_{\mathbf{W}_p}^2$$
$$+ \frac{\rho}{2}\|\mathrm{B}_p(\delta\mathbf{n}) - \mathbf{v}_p + \mathbf{w}_p/\rho\|_2^2 + \tau\|\delta\mathbf{n}\|_{\text{TV}}, \quad (10)$$

where $\mathbf{w}_p$ and ρ are the Lagrangians and the penalty parameter [14]. Algorithm 1 shows the steps to minimize (10) using ADMM.

Algorithm 1 ADMM for minimizing (10)

Require: $\{\mathbf{y}_p\}_{p\in[1\ldots P]},\ \delta\mathbf{n}^{(0)} \in \mathbb{R}_{\geq 0}^N, \rho > 0, \tau > 0$
1: $\mathbf{w}_p^{(0)} = \mathbf{0}_{\mathbb{C}^{N_x}},\ \forall p \in [1 \ldots P]$
2: $k = 0$
3: **while** (not converged) **do**
4: $\quad \mathbf{v}_p^{(k+1)} = \text{prox}_{\frac{1}{2\rho}\||\cdot|^2 - \mathbf{y}_p\|_{\mathbf{W}_p}^2}\left(\mathrm{B}_p(\delta\mathbf{n}^{(k)}) + \frac{\mathbf{w}_p^{(k)}}{\rho}\right)$
5: $\quad \delta\mathbf{n}^{(k+1)} = \arg\min_{\delta\mathbf{n}\in\chi}\left(\frac{1}{2}\sum_{p=1}^{P}\|\mathrm{B}_p(\delta\mathbf{n}) - \mathbf{v}_p^{(k+1)} + \frac{\mathbf{w}_p^{(k)}}{\rho}\|_2^2 + \frac{\tau}{\rho}\|\delta\mathbf{n}\|_{\text{TV}}\right)$
6: $\quad \mathbf{w}_p^{(k+1)} = \mathbf{w}_p^{(k)} + \rho(\mathrm{B}_p(\delta\mathbf{n}^{(k+1)}) - \mathbf{v}_p^{(k+1)}),\ \forall p \in [1 \ldots P]$
7: $\quad k \leftarrow k + 1$
8: **end while**
9: **return** $\delta\mathbf{n}^{(k)}$

3.1. Proximity Operator

At Step 4 of Algorithm 1, one has to compute the proximity operator of $\mathcal{D}(\mathbf{v}) = \frac{1}{2\rho}\||\mathbf{v}|^2 - \mathbf{y}_p\|_{\mathbf{W}_p}^2$ defined as

$$\text{prox}_{\mathcal{D}}(\mathbf{x}) = \arg\min_{\mathbf{v}\in\mathbb{C}^{N_x}}\left(\frac{1}{2}\|\mathbf{v} - \mathbf{x}\|_2^2 + \mathcal{D}(\mathbf{v})\right). \quad (11)$$

Here, we take advantage of the closed-form expressions that have been recently derived for both Gaussian and Poisson likelihoods in [15]. Specifically, the proximity operator in (11) is computed component-wise according to

$$\forall \mathbf{x} \in \mathbb{C}^{N_x},\ [\text{prox}_{\mathcal{D}}(\mathbf{x})]_m = \varrho_m\, \mathrm{e}^{\mathrm{j}\arg(x_m)}, \quad (12)$$

where ϱ_m is the positive root of the 3rd degree three polynomial

$$q_G(\varrho) = \frac{4w_m^p}{\rho}\varrho^3 + \varrho\left(1 - \frac{4w_m^p}{\rho}[\mathbf{y}_p]_m\right) - |x_m|, \quad (13)$$

which is found with Cardano's method.

3.2. Solving for $\delta\mathbf{n}$

At Step 5 of Algorithm 1, we need to reconstruct the RI distribution from the complex "data" $\mathbf{z}_p^{(k+1)} = \mathbf{v}_p^{(k+1)} - \mathbf{w}_p^{(k)}/\rho$, taking into account that

$$\delta\mathbf{n}^{(k+1)} = \arg\min_{\delta\mathbf{n}\in\chi}\left(\frac{1}{2}\sum_{p=1}^{P}\|\mathrm{B}_p(\delta\mathbf{n}) - \mathbf{z}_p^{(k+1)}\|_2^2 + \frac{\tau}{\rho}\|\delta\mathbf{n}\|_{\text{TV}}\right). \quad (14)$$

This optimization problem is solved using the fast iterative shrinkage-thresholding algorithm (FISTA) [16], which has already been proven to be useful in this context [17, 6]. Two quantities are required

1. The proximity operator of $\frac{\tau}{\rho}\|\cdot\|_{\mathrm{TV}}$ which is computed efficiently using a standard iterative method [6].
2. The gradient of $\mathcal{F}(\delta\mathbf{n}) = \frac{1}{2}\sum_{p=1}^{P}\|\mathrm{B}_p(\delta\mathbf{n}) - \mathbf{z}_p^{(k+1)}\|_2^2$ which is derived using classical differential rules.

Specifically, we have that

$$\nabla\mathcal{F}(\delta\mathbf{n}) = \sum_{p=1}^{P}\mathrm{Re}\left(\mathbf{J}_{\mathrm{B}_p}^{H}(\delta\mathbf{n})(\mathrm{B}_p(\delta\mathbf{n}) - \mathbf{z}_p^{(k+1)})\right), \tag{15}$$

where $\mathbf{J}_{\mathrm{B}_p}(\delta\mathbf{n})$ is the Jacobian matrix of the BPM forward model. It is computed efficiently by back-propagation as in [6].

Moreover, to reduce the computational cost, we compute the gradient only from a subset of angles $L < P$. We choose the angles such that they are equally spaced and increment them at each FISTA iteration. The computational complexity of $\nabla\mathcal{F}(\delta\mathbf{n})$ for one angle corresponds to the cost of $6N_z$ FFTs of size N_x.

We implemented Algorithm 1 using the GlobalBioIm library [18].

4. NUMERICAL EXPERIMENTS

4.1. Simulated data

We simulated intensity measurements using a nonlinear accurate forward model [19]. The square area $\Omega = 33\lambda \times 33\lambda$ includes the sample and the sensors. The medium has a RI $n_b = 1.33$ (*i.e.,* water). The setup is similar to the scheme in Figure 1. A cell-like phantom is included in a central area of side 16.5λ. As shown in Figure 2 (top left), the cell body and the two ellipses have a RI of 1.355, 1.432 and 1.457 respectively. We simulated on a very fine grid in order to reduce numerical errors (*i.e.,* 1024×1024) and then down-sampled (512×512) to get the measurements used for the reconstruction (last column of this matrix). The plane waves have incident angles equally spaced between $-\frac{\pi}{4}$ and $\frac{\pi}{4}$. Thirty one sets of measurements were acquired with a wavelength of 406 nm (*i.e.,* $P = 31$). The reconstruction problem is challenging because of the limited-angle illuminations (missing cone). We computed the reconstruction error $\frac{\|\delta\mathbf{n}-\delta\mathbf{n}_{true}\|_F}{\|\delta\mathbf{n}_{true}\|_F}$ with $\|\cdot\|_F$ the Frobenius norm.

Our reference is the (linear) light field refocusing (LFR) method [20] which is also used to initialize Algorithm 1. It provides a reasonably "good" start, which is crucial here since the optimization task is non-convex. The algorithm parameters were manually set to $\rho = 10^{-3}$, $L = 8$ and the step size in FISTA to $\gamma = 5 \cdot 10^{-4}$.

Noiseless measurements For this experiment, we set the regularization parameter to $\tau = 1.5 \cdot 10^{-6} \cdot \|\mathbf{y}_{P/2}\|_2^2$. We compare the proposed method with the BPM method in [6] that reconstructs the RI map from holographic measurements (BPMc). We initialize this algorithm with a filtered back-projection method (FBP) [21]. As shown in Figure 2, the proposed method is able to recover the RI distribution. One can observe that the structures are slightly elongated along z, as a consequence of the missing cone. However, contrarily to the LFR solution, we can distinguish the two ellipses and the shape of the cell body. The reconstructed RI is also close to the true value. The reconstruction error is $6 \cdot 10^{-3}$. The proposed method compares well against BPMc (error $5.4 \cdot 10^{-3}$) for which the phase was provided.

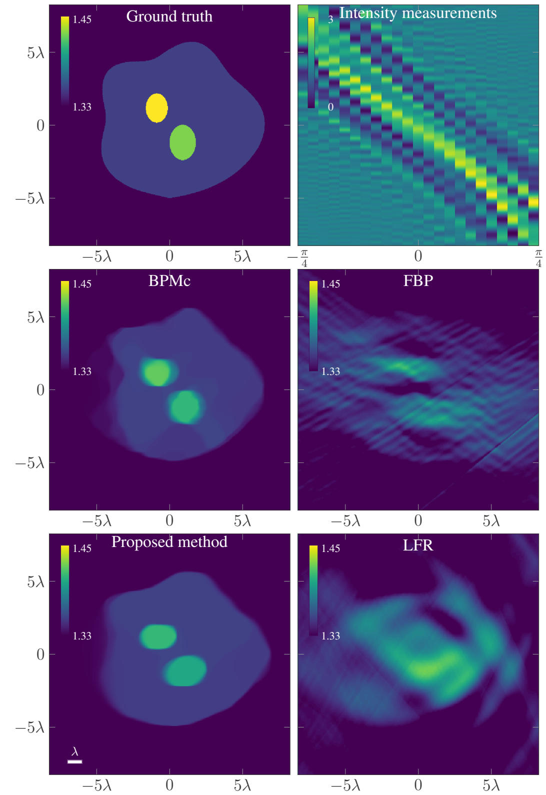

Fig. 2. Simulated data and their reconstruction. From left to right: (top) the cell-like phantom and its associated noiseless intensity measurements; (middle) the solutions from FBP [21] and BPMc [6]; (bottom) the LFR solution [20], and the RI distribution recovered by the proposed method. The elongated ellipses are due to missing informations along the optical axis.

Noisy measurements We simulated noisy measurements at three different noise levels. For each of them, we set the incident fields $(\mathbf{u}_p^{\mathrm{in}})_{p\in[1...P]}$ such that $|[\mathbf{u}_p^{\mathrm{in}}]_m| = A \in \mathbb{R}_{>0}$ and simulated the resulting intensity measurements. We considered three scenarios with $A = 1.75, 3$ and 5. Then, these measurements were corrupted using a Poisson distribution. The resulting SNR are 5.32, 9.77 and 14.13 dB, respectively. Simulated measurements are shown in Figure 3 (top line). The regularizations were set to $\tau = 10^{-6} \cdot \|\mathbf{y}_{P/2}\|_2^2$ for all noise levels.

As shown in Figure 3 (bottom line), the proposed method is still able to recover the shape of the cell and the ellipses. The reconstruction errors are $9.47 \cdot 10^{-3}$, $8.07 \cdot 10^{-3}$ and $6.17 \cdot 10^{-3}$ for $A = 1.75, 3$ and 5, respectively. Despite the noise, we can still distinguish the different elements of the phantom, which demonstrates the robustness of the method.

4.2. Experimental data

We validated our method on experimental data. Holographic measurements were collected using a standard Mach-Zehnder interferometer, which relies on off-axis digital holography ($\lambda = 450$ nm). The sample was the cross-section of two fibres immersed in a medium of RI $n_b = 1.525$ (oil). We obtained $P = 160$ views ranging from $-\frac{\pi}{4}$ to $\frac{\pi}{4}$. The RI variation is negative $\delta\mathbf{n} \in \mathbb{R}_{\leq\mathbf{0}}$. The reconstructed area is $\Omega = 38\lambda \times 97\lambda$. We compare the performance of the proposed method with BPMc. The latter and Algorithm 1 were

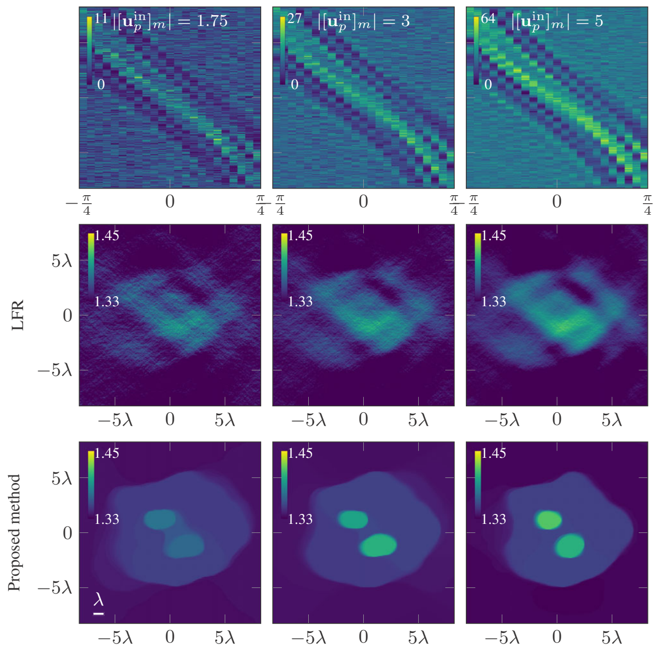

Fig. 3. Noisy measurements and their RI reconstructions. Each column corresponds to a noise level. From left to right: $|[\mathbf{u}_p^{in}]_m| = 1.75$, $|[\mathbf{u}_p^{in}]_m| = 3$, $|[\mathbf{u}_p^{in}]_m| = 5\ \forall p \in [1 \dots P]$. Top to bottom: intensity measurements, LFR [20], and proposed method.

initialized with the solutions of the Rytov based-backpropagation [3] and LFR respectively.

The FISTA step size was set at $\gamma = 0.2/\|\mathbf{y}_{P/2}\|_2^2$ for BPMc and our method. We set the penalty parameter to $\rho = 2.5$ for Algorithm 1. The regularization parameter τ was tuned manually.

As shown in Figure 4, both BPMc and the proposed method are able to reconstruct the cross-section of the two fibres. Although the phase is missing, our method reaches performances similar to BPMc.

5. CONCLUSION

We have proposed a method to reconstruct a map of refractive index (RI) from intensity-only measurements. It is a non-trivial extension from complex to amplitude-only of a state-of-the-art method for RI reconstruction from holographic measurements. We have combined proximity operators for phase retrieval with an efficient RI reconstruction pipeline. Using an adequate splitting of the problem, our method can cope with different noise models and regularizers. We showed its robustness to noise and to the limited-angle acquisition settings that are the main difficulties for biological imaging.

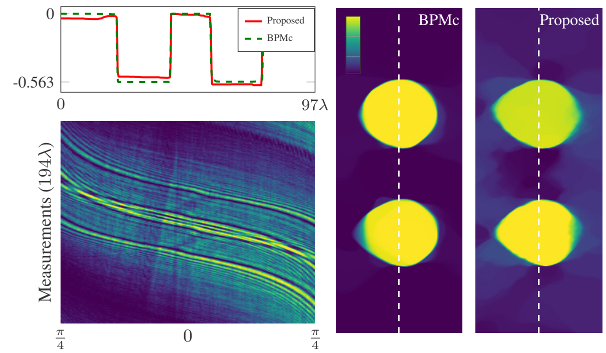

Fig. 4. RI reconstructions of two fibres. Top left: profile plots of reconstructions from BPMc and proposed method of the dashed lines on the right. Bottom left: intensity measurements experimentally acquired. Right: BPMc (complex measurements) and proposed method (intensity measurements).

6. REFERENCES

[1] D. Jin, R. Zhou, Z. Yaqoob, and P. T. C. So, "Tomographic phase microscopy: Principles and applications in bioimaging," *Journal of the Optical Society of America B*, vol. 34, no. 5, pp. B64–B77, May 2017.

[2] E. Wolf, "Three-dimensional structure determination of semi-transparent objects from holographic data," *Optics Communications*, vol. 1, no. 4, pp. 153–156, September 1969.

[3] A. J. Devaney, "Inverse-scattering theory within the Rytov approximation," *Optics Letters*, vol. 6, no. 8, pp. 374–376, August 1981.

[4] Y. Sung, W. Choi, C. Fang-Yen, K. Badizadegan, R. R. Dasari, and M. S. Feld, "Optical diffraction tomography for high resolution live cell imaging," *Optics Express*, vol. 17, no. 1, pp. 266–277, January 2009.

[5] J. Lim, K. Lee, K. Jin, S. Shin, S. Lee, Y. Park, and J. C. Ye, "Comparative study of iterative reconstruction algorithms for missing cone problems in optical diffraction tomography," *Optics Express*, vol. 23, no. 13, pp. 16933–16948, June 2015.

[6] U. S. Kamilov, I. N. Papadopoulos, M. H. Shoreh, A. Goy, C. Vonesch, M. Unser, and D. Psaltis, "Optical tomographic image reconstruction based on beam propagation and sparse regularization," *IEEE Transactions on Computational Imaging*, vol. 2, no. 1, pp. 59–70, January 2016.

[7] U. S. Kamilov, D. Liu, H. Mansour, and P. T. Boufounos, "A recursive Born approach to nonlinear inverse scattering," *IEEE Signal Processing Letters*, vol. 23, no. 8, pp. 1052–1056, August 2016.

[8] R. Gerchberg and W. O. Saxton, "A practical algorithm for the determination of phase from image and diffraction plane pictures," *Optik*, vol. 35, pp. 237, November 1972.

[9] G. Zheng, R. Horstmeyer, and C. Yang, "Wide-field, high-resolution Fourier ptychographic microscopy," *Nature Photonics*, vol. 7, no. 9, pp. 739–745, July 2013.

[10] L. Tian, X. Li, K. Ramchandran, and L. Waller, "Multiplexed coded illumination for Fourier ptychography with an LED array microscope," *Biomedical Optics Express*, vol. 5, no. 7, pp. 2376–2389, July 2014.

[11] A. M. Maiden, M. J. Humphry, and J. M. Rodenburg, "Ptychographic transmission microscopy in three dimensions using a multi-slice approach," *Journal of the Optical Society of America A*, vol. 29, no. 8, pp. 1606–1614, August 2012.

[12] L. Tian and L. Waller, "3D intensity and phase imaging from light field measurements in an LED array microscope," *Optica*, vol. 2, no. 2, pp. 104–111, February 2015.

[13] P. Li, D. J. Batey, T. B. Edo, and J. M. Rodenburg, "Separation of three-dimensional scattering effects in tilt-series Fourier ptychography," *Ultramicroscopy*, vol. 158, pp. 1–7, November 2015.

[14] S. Boyd, N. Parikh, E. Chu, B. Peleato, and J. Eckstein, "Distributed optimization and statistical learning via the alternating direction method of multipliers," *Foundations and Trends in Machine Learning*, vol. 3, no. 1, pp. 1–122, January 2011.

[15] F. Soulez, E. Thiébaut, A. Schutz, A. Ferrari, F. Courbin, and M. Unser, "Proximity operators for phase retrieval," *Applied Optics*, vol. 55, no. 26, pp. 7412–7421, September 2016.

[16] A. Beck and M. Teboulle, "A fast iterative shrinkage-thresholding algorithm for linear inverse problems," *SIAM Journal on Imaging Sciences*, vol. 2, no. 1, pp. 183–202, March 2009.

[17] U. S. Kamilov, I. N. Papadopoulos, M. H. Shoreh, A. Goy, C. Vonesch, M. Unser, and D. Psaltis, "Learning approach to optical tomography," *Optica*, vol. 2, no. 6, pp. 517–522, June 2015.

[18] M. Unser, E. Soubies, F. Soulez, M. McCann, and L. Donati, "GlobalBioIm: A unifying computational framework for solving inverse problems," in *Proceedings of the OSA Imaging and Applied Optics Congress on Computational Optical Sensing and Imaging (COSI'17)*, San Francisco CA, USA, June 26-29, 2017, paper no. CTu1B.

[19] E. Soubies, T.-A. Pham, and M. Unser, "Efficient inversion of multiple-scattering model for optical diffraction tomography," *Optics Express*, vol. 25, no. 8, pp. 21786–21800, September 4, 2017.

[20] G. Zheng, C. Kolner, and C. Yang, "Microscopy refocusing and dark-field imaging by using a simple LED array," *Optics Letters*, vol. 36, no. 20, pp. 3987–3989, October 2011.

[21] A. Kak and M. Slaney, *Principles of computerized tomographic imaging*, SIAM, 2001.